Check for updates

Recent advances of polyoxometalates in multi-functional imaging and photothermal therapy

Xueping Kong, Guofeng Wan, Bao Li (ID) and Lixin Wu (ID) *

Polyoxometalates (POMs) as a kind of molecular metal-oxide cluster with precise chemical composition and architecture have been demonstrated to show potential in multidisciplinary materials. Accompanied by their bioactivities, POM clusters have also been shown to be capable of sensing diseases and allowing synergistic therapy based on their redox and near infrared absorption. In parallel with metal nano-particles and organic materials, these inorganic clusters have also displayed unique photothermal imaging and therapeutic properties over recent years. In this review, we outlined the main achievements of POMs in the fields of bio-detecting probes and the photothermal effect. Fluorescence detection, magnetic resonance, computed tomography, and photothermal property-supported photoacoustic imaging acting as a multifunction platform that integrates photothermal therapy (PTT) were discussed at the same time. The comparison of nanocomposites to POMs alone in imaging-guided PTT, multi-modal imaging, and the combination of PTT with controlled chemotherapy and gas therapy were described in detail. The advantages and possible drawbacks of POMs as well as perspectives in related areas were analyzed, which ascertained such clusters to be a type of promising agent in biomedical applications.

1. Introduction

Rapid developments in accurate medicine and life science require precise diagnosis at the levels of cells, tissues, organs, and human bodies. High-resolution visualization methods toward meeting the challenge have proved to be promising approaches and various radiation techniques have been exploited in the past decades. Typically, a variety of imaging methods have been developed to examine physiological and pathological changes

State Key Laboratory of Supramolecular Structure and Materials, College of Chemistry, Jilin University, Changchun, 130012, China. E-mail: wulx@jlu.edu.cn

through the modulation of the organism response to external stimuli, such as light[1,2] and electric signals,[3] radiation,[4] magnetic fields,[5] *etc.* In addition to the early used methods, recently applied imaging modalities include photoluminescence (PL) imaging, magnetic resonance imaging (MRI), positron emission tomography (PET), photoacoustic imaging (PAI), computed tomography (CT), ultrasound (US) imaging, thermal imaging (TI) and so on. The imaging modalities can be roughly divided into two categories according to their characteristics. MRI, US, PAI and CT are classified as morphological/anatomical imaging techniques with high spatial resolution, while PL, PET and TI are categorised as molecular imaging routes by detecting

Xueping Kong received her BS degree in chemistry from Jilin University in 2017 and won the honourable qualification to be a postgraduate student with exemption from the national tests. She then joined Prof. Lixin Wu's group at Jilin University and now her research project lies in the multi-functional imaging and treatment of polyoxometalate-based hybrid materials.

Xueping Kong

Guofeng Wan received his BS degree from Jilin University in 2018 and won the honourable qualification to be a postgraduate student with exemption from the national tests. He then joined Prof. Lixin Wu's group at Jilin University for a PhD degree. His research concerns polyoxometalate-based complexes for drug delivery and bioimaging.

Guofeng Wan

molecular and cellular changes.[6,7] However, both imaging methodologies display pivotal advantages and inevitable defects and thus the combination of various imaging modalities to achieve complementary advantages for more accurate results becomes highly desired. On the other hand, the integration of imaging with therapy points out the most promising tendency to push the diagnosis to the final targeted treatment in the form of more effective and less harmful treatment for the organism. The great progress of biomaterials, especially functional nanomaterials, provides unlimited opportunities.

The photothermal effect as an important physical phenomenon that transforms photoenergy to heat through a non-radiative transition has been known for a long period, but it was not really developed for medical diagnosis, until lately it was observed in some semiconductor nanomaterials with high transduction efficiency.[8] As a non-invasive and topical approach, this effect becomes very important both in bioimaging and therapy *via* a vein or local injection and has attracted wide attention. In targeted photothermal therapy (PTT), the hyperthermia yielded from the energy transfer of a remote light source to the local photosensitizer kills the anchored tumour cells.[9] Given the nano- and/or molecular structure, a variety of organic and inorganic hybrid materials were tried to be used for photosensitizers to achieve a high temperature within a few minutes under laser irradiation. In comparison to other imaging techniques, the photothermal imaging (PTI) method is less dependent on expensive and complicated instruments but primarily concerned with the materials used. In addition, the rational design of materials allows the chemical objects serving as probes to possess multiple functions for targeting, imaging and therapeutic effects.[10] Therefore, location recognizing therapy accompanied by imaging guidance to kill cancer cells efficiently while avoiding damage to normal tissues will be one of the critical strategies. But still, finding suitable nanomaterials with the features of nontoxicity, biocompatibility, precise chemical structure and stability, and high photothermal conversion efficiency is essential prerequisite.

Some typical inorganic metal nanoparticles, graphene and carbon materials, and conjugated organic and polymer materials showing photothermal phenomena have been reviewed in recent years.[11–13] In comparison to these photothermal materials, polyoxometalates (POMs) as a class of polyanionic clusters comprised of early-transition-metal oxides exhibit abundant chemical compositions and rich nanosized architectures. Their diverse physicochemical properties endow POMs with significant potential in photo-, electro-, and magnetic materials, catalysis, and biological systems.[14–17] The antibacterial and antitumor properties of POMs have been extensively studied,[18,19] while the role played in molecular imaging and various therapeutics remains to be exploited. More importantly, in recent years, the application of POMs in PTT has attracted attention, whereas the systematic summaries on these bio-applications are very rarely reported.[20] Considering the outstanding performance of POMs in PTT and the rapid development, it is worth collecting the recent advances in photothermal transduction and integration with other imaging techniques for bimodal or multiple therapeutic applications. Therefore, we herein would like to give a systematic outline disclosing the working progress in the budding field. In this review, multifunctional imaging features and the photothermal properties related to PTT and PAI of POMs for accurate diagnosis and targeting were discussed. Additionally, the integration of the PTT property of POMs with chemotherapy and gas therapy was described for achieving better therapy outcomes. We believe that these recent instructive for further research toward practical applications.

2. POMs for biological imaging

2.1 Basis of multiple imaging methods

The imaging methodologies used in bio-detection are based on the physical and chemical principles occurring in organisms with or without additive agents. Though detailed descriptions have been systematically summarized in many specialized reviews,[21]
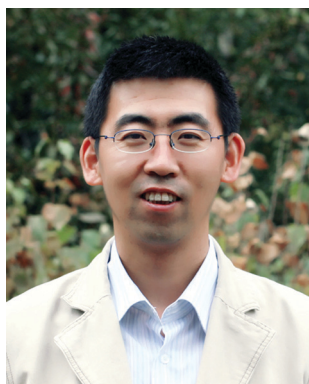
Bao Li

Dr Bao Li is now Associate Professor of Chemistry at Jilin University. He gained his BS degree in 2003 and PhD degree in polyoxometalate chemistry from Jilin University in 2008 under the supervision of Prof. Lixin Wu. His current research interests focus on the synthesis of organically grafted polyoxometalates and applications of inorganic clusters in chiral self-assembly, selective adsorption and bioimaging.

Lixin Wu

Dr Lixin Wu is now a Professor in the State Key Laboratory of Supramolecular Structure and Materials at Jilin University. He received his PhD degree in physical chemistry from Jilin University in 1993 and experienced senior postdoctoral fellow (JSPS) training at Hokkaido University and research associate work at University of Hong Kong from 1996 to 1998. His current research topics involve self-assembly and supramolecular chemistry, polyoxometalate synthesis, and bio-applicable hybrid polymer materials.

a brief introduction is still necessary for understanding the fundamental background of the imaging methods dealt with here, especially the photothermal effect.

CT imaging based on X-ray photography based on the X-ray penetration in three dimensions is characterized by high spatial resolution, which provides complementary anatomical information to distinguish different tissues.[22] Biological human tissues and organs are composed of a variety of substances with different atomic numbers and electronic densities, resulting in differentiated attenuation coefficients for X-ray radiation. When the applied X-ray passes through a certain thickness of the inspection site, the obtained signal of the detected X-ray through the layer is then processed to obtain the CT image.[23] In most cases, no additional agents are required for enhanced contrast, but iodine-based molecules were used sometimes to stain different types of soft tissues during imaging.[24] Limited by the short circulation time of iodinated contrast agents, other nanoparticles containing elements with high atomic number, such as gadolinium,[25] bismuth,[26] gold,[27] tungsten,[28] and so forth, were used in CT imaging, providing opportunities for multiple detections together with MRI, FL and PTI at the same time.

As another high-resolution and non-invasive imaging modality with great clinical importance, MRI has been adopted widely due to it being almost harmless to human bodies. MRI is based on the precession of water hydrogen nuclei within an applied external magnetic field.[29] After application of radiofrequency pulses, the relaxation process through which the nuclei return to the original aligned state can be exploited to produce an image. The relaxation process involves the longitudinal relaxation time (T_1) and the transverse relaxation time (T_2), both of which can be used to generate MR images.[30] Like the CT method, MRI also has the ability to obtain a tomographic image in any direction, benefiting from its good spatial resolution in three-dimensions (3D). In general, MRI suffers from low sensitivity, especially for some moving organs, and the scanning takes quite a long time. In the case of precise and enhanced imaging, paramagnetic, superparamagnetic and ferromagnetic MRI contrast agents regarding the detection requirement have to be used. Gadolinium chelates, iron oxides and some manganese compounds with high relaxation rates are the commonly used contrast agents.[31–33]

The light imaging signals based on additive molecular probes mainly use the absorption and emission principles of molecules or semiconductors in the presence of ultraviolet, visible, infrared, and near infrared light radiation. The contrast derives from the density variation of the molecular probes between different tissues. According to the general photophysical process, when a molecule absorbs light, one of its electrons located in the highest occupied molecular orbital in the ground state will be excited to jump into the empty orbitals in the excited state. The excited electron goes back to the lowest excited energy level S_1 very quickly with the release of thermal energy. At this time, there are two possible routes for the electron going back to the ground state: one is to emit long wavelength light and the other route is to lose the energy via a
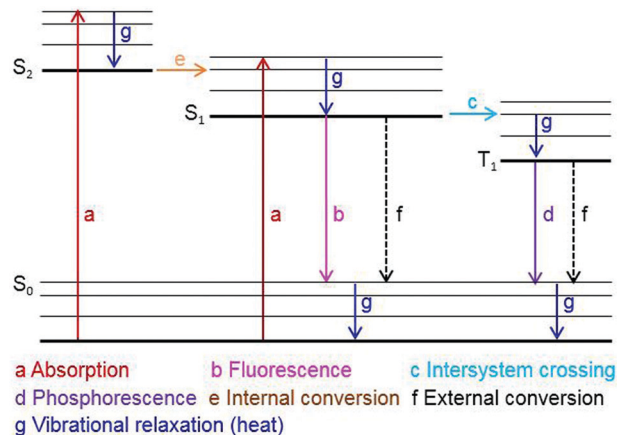

Fig. 1 Schematic illustration of possible relaxation paths of light-excited energy back to the ground state via luminescence, heat and phosphorescence as a Jablonski plot.

non-radiative transition by releasing heat.[34] There are several non-luminescence approaches including non-radiative transitions, vibrational relaxations, and internal and external conversion which lead to the production of heat. Of course, there are other photophysical behaviours which are not discussed here due to their lower possibility to be used in imaging except phosphor luminescence. The basic principle can be expressed by the Jablonski plot in Fig. 1.[35] When the luminescence quantum yield in the visible wavelength range becomes very high, molecules can be potentially used as fluorescence imaging probes through injection into organisms. Meanwhile, when the heat yielded from various non-radiative transitions accumulates to result in a quick temperature increase, the molecular materials become suitable for thermal imaging and high-photothermal conversion provides features for therapy. A requisite condition for all these performances is that the materials have to possess a high absorption coefficient, which contributes to the high transition probability of electrons under radiation at the selected wavelength.

Apparently, the photoluminescence and photothermal effects are competitive processes with each other during excited energy relaxation, and it is almost impossible for single component materials to show both strong characteristics at the same time.[36] However, the two mutually inhibiting imaging techniques are compatible with CT and MRI images. Therefore, a suitable combination of the photothermal effect with other imaging principles can lead to multiple imaging functions and a combination of therapeutic effects. FI is adopted as a powerful and non-invasive analytical tool for visualizing biological species by virtue of its fast response, excellent temporal resolution, superb sensitivity, in situ workability, simple operation, and good reproducibility.[37] However, FI suffers from poor tissue penetration and this modality is highly susceptible to background noise due to tissue scattering of photons in the visible light region (395–600 nm).[38,39] To overcome the intrinsic limitations, more and more attention was paid to moving FI to the near infrared region (NIR, 700–1700 nm), and the fluorescence of contrast agents in this wavelength range helps to achieve more sensitive imaging.

The near infrared biological window is usually divided into two regions, the first is named NIR-I (700–1000 nm) and the second is called NIR-II (1000–1700 nm). Compared to the FI bio-window at NIR-I, NIR-II FI is more ideal for *in vivo* imaging with deeper tissue penetration, higher temporal resolution, better spatial resolution, and lower background noise, which has been reviewed before.[40–42]

2.2 POMs for multiple imaging

Because of the structural and bond properties, almost all POMs comprising early transition metals in the highest oxidation state are non-luminescent. But a large fraction of POMs can be modified through replacing one or more W/Mo atoms with transition or rare earth metal ions to show strong emission *via* the charge transfer transition. The lanthanide-containing POMs, such as $K_{13}[Eu(\beta_2-SiW_{11}O_{39})_2] \cdot 25H_2O$ and $Na_9[Eu(W_5O_{18})_2] \cdot 32H_2O$, exhibit typical photoluminescence of the rare earth metal complexes in the visible region, large Stokes shift, and long lifetime of the excited states.[43] In all present luminescent POMs containing rare earth metals, the terminal oxygen atoms at the lacunary position provide the coordination sites and the POMs play the role of ligands. Therefore, there is an energy transfer of oxygen to metals and then to rare earth metals, which greatly raises the quantum yield. However, the naked clusters were rarely used directly in *in vivo* imaging owing to their strong quenching in aqueous solution,[44,45] though the quenching effect of certain POMs was used for quantitative detection.[46] To overcome the unfavourable factor, Eu-containing POMs were enwrapped with biocompatible molecules to restrict the competitive coordination from water molecules, achieving physiological stability and maintaining the lifetime in water.[47,48] Biocompatible nanoparticles with luminescent properties were synthesized by encapsulating a nano-scale assembly of $Na_9[Eu(W_5O_{18})_2] \cdot 32H_2O$ with *in situ*-polymerized acrylic acid (PAA) (abbreviated as $EuW_{10}@PAA$), and then conjugated with a mitochondria-targeting peptide to form $EuW_{10}@PAA$ nanoparticle–peptide conjugates (NP–peptide), as shown in Fig. 2. FI characterization confirmed that NP–peptide can be successfully delivered into mitochondria with high efficiency compared with bare clusters, which was verified by Bio-TEM results in Fig. 2d and e. The dynamic intracellular behaviours of NP–peptide conjugates regarding how they were transported and changed their time-course distribution inside cells were concluded from the distribution of the POM's fluorescence intensity.[49]

On the other hand, similar substitutions of rare earth metals in POMs can lead to contrast agents based on another imaging principle as given in Table 1. Gadolinium ion (Gd^{3+}) complexes are generally chosen as T_1 contrast agents because of their large paramagnetic moment and long electronic relaxation time, which can effectively shorten the T_1 of water protons, thus achieving enhanced relaxivity (r_1) and realizing a brighter contrast effect.[50] Compared with commercial contrast agents, rare earth Gd^{3+}-based chelate compounds, like POMs incorporated with Gd^{3+}, have been reported to exhibit enhanced MRI contrast owing to the greatly increased molecular weight and rigid framework architecture.[51–55] Though the imaging derives from POMs, they were still coated with a cationic surfactant or polymers to improve the stability and biocompatibility in the physiological environment. POMs in the form of ionic complexes can generate a longer rotational correlation time and an enhanced r_1, while the proton exchange between bulk water and the coordinated water of POMs is not blocked *via* a suitable structure design. As an example, the relaxivity is greatly improved
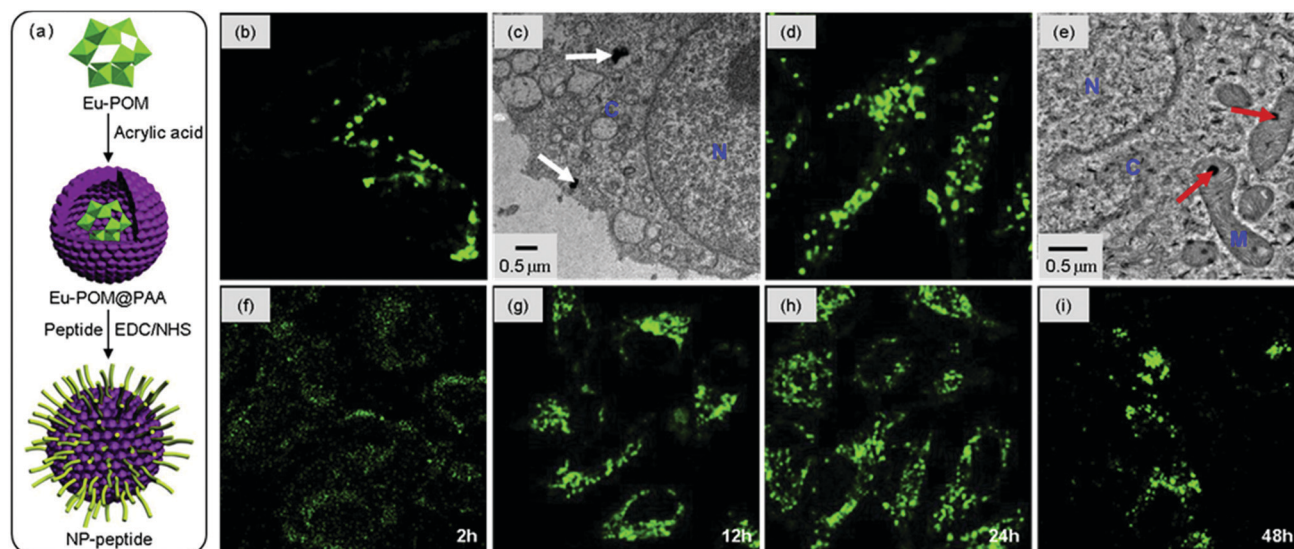

Fig. 2 (a) Schematic illustration of the synthetic procedures of NP–peptide. CLSM images and corresponding Bio-TEM images of MCF-7 cells incubated for 12 h with (b and c) bare nanoparticles and (d and e) NP–peptide at a concentration of 50 µg mL^{-1}, where the arrows point to accumulation of the corresponding nanoparticles and the nucleoplasm is (N), cytoplasm is (C), and mitochondria are (M). CLSM images of MCF-7 cells sourced from incubation of 50 µg mL^{-1} NP–peptide for (f) 2 h, (g) 12 h, (h) 24 h and (i) 48 h. Reprinted with permission from ref. 49. Copyright 2015, American Chemical Society.

Table 1 The summary of POMs and their composites acting as contrast agents for MRI in recent work

POMs/POM composites	Added property	Size	Concentration	Condition	Time	Ref.
$K_{13}[Gd(\beta_2\text{-}SiW_{11}O_{39})_2]$ covered with cationic poly(ethylene oxide)	N/A	~160 nm	N/A	*In vitro*	2012	51
$K_{13}[Gd(\beta_2\text{-}SiW_{11}O_{39})_2]$ covered with dendritic cations (D-1)/(D-2)	N/A	144/165 nm	0.92 mmol per kg body weight	*In vivo*	2017	52
$K_9GdW_{10}O_{36}$ $K_{11}[Gd(PW_{11}O_{39})_2]$	N/A	N/A	0.087 ± 0.005 0.092 ± 0.002 mmol kg^{-1} Gd per kg body weight	*In vivo*	2002	53
$KCs_4[Gd(\alpha\text{-}SiW_{11}O_{39})]\cdot25H_2O$ $K_{13}[Gd(\beta_2\text{-}SiW_{11}O_{39})_2]\cdot27H_2O$	N/A	N/A	N/A	*In vitro*	2013	54
$Gd_2P_2W_{18}O_{62}$ $K_{15}[(GdO)_3(PW_9O_{34})_2]$	N/A	N/A	0.091 ± 0.013, 0.081 ± 0.013 mol kg^{-1} Gd per kg body weight	*In vivo*	2002	55
$Na_9[GdW_{10}O_{36}]$ covered with cationic (poly(hexylspermine)acrylamide)	N/A	70 nm	N/A	*In vitro*	2013	56
$Na_9[GdW_{10}O_{36}]$ covered with PDMAEMA$_{20}$ (P$_{20}$)	N/A	11–13.5 nm	N/A	*In vitro*	2018	57
$[Mn_{12}O_{12}(O_2CCH_3)_5(O_2CC_{17}H_{35})_{11}(H_2O)]$	N/A	75 ± 30 nm	N/A	*In vitro*	2011	61
GdW$_{10}$@BSA@Ti$_3$C$_2$	PTT	~309 nm	20 mg kg^{-1} body weight	*In vivo*	2018	64
$K_{13}[Gd(\beta_2\text{-}SiW_{11}O_{39})_2]$ covered with dendritic cations (D-3)	Fluorescence	5.6 ± 1.5 nm	1.5 mmol kg^{-1} body weight	*In vivo*	2017	65
BSA-coated $Na_9[GdW_{10}O_{36}]$	PTT@radiotherapy	~3.5 nm	75 µmol kg^{-1} body weight	*In vivo*	2016	83

when external molecules with small molecular weight cover POMs in terms of the *in vitro* T_1-weighted MR images, as shown in Fig. 3a.[52] With this method, the relaxivity of $Na_9[Gd(W_5O_{18})_2]$ (GdW$_{10}$) was enhanced about 3 times when incorporating it into a cationic polymer [poly(hexylspermine)acrylamide] through electrostatic interactions.[56] The r_1 value of nano-assemblies formed from GdWO and cationic mPEG brush block copolymer PDMAEMA$_{20}$ (P$_{20}$) was found to be dependent on the charge ratio rather than the chain length of the cationic polymer block,

indicating the critical role of the ionic interaction, as presented in Fig. 3b.[57] Unlike T_1 MR imaging, which promotes the spin–lattice relaxation of protons, directing a positive (or bright) MR image, T_2 MR imaging causes surrounding protons to undergo spin–spin relaxation and gives rise to negative (or dark) MR images.[58–60] Particularly, single-molecule magnet $Mn_{12}O_{12}(OOCR)_{16}$ (Mn$_{12}$) can be used in T_2 imaging, as the induced magnetic moment in the applied field can accelerate the relaxation of water protons in its vicinity.[61]

Fig. 3 (a) Schematic chemical structures of two different dendritic cation-encapsulated Gd ion-substituted POM complexes and the pseudo-colour diagrams of *in vitro* T_1-weighted MR images for the GdSiW$_{11}$ cluster, and (D-1)$_{13}$GdSiW$_{11}$ and (D-2)$_{13}$GdSiW$_{11}$ complexes. Reprinted with permission from ref. 52. Copyright 2017, Royal Society of Chemistry. (b) Schematic illustration of nano-assemblies formed from GdWO and cationic brush block copolymer mPEG, PDMAEMA$_{20}$ (P$_{20}$), and T_1-weighted MRI phantom images of Gd-DTPA, GdWO and the selected nano-assemblies $^{0.2}$P$_{20}$@GdWO and $^{0.3}$P$_{20}$@GdWO at pH 7.4 and pH 6.0. Reprinted with permission from ref. 57. Copyright 2018, Royal Society of Chemistry.

This journal is © The Royal Society of Chemistry 2020

J. Mater. Chem. B, 2020, **8**, 8189–8206 | 8193

Table 2 The summary of POMs and their composites acting as contrast agents for FI and CT imaging in recent work

	POMs/POM composites	Added property	Size	Concentration	Condition	Pub. year	Ref.
FI	$[C_{16}\text{-}2\text{-}C_{16}im]Br_2/Eu\text{-POM hybrid}$	N/A	50–100 nm	N/A	*In vitro*	2016	43
	$[(DOHDA)_6H_3EuW_{10}O_{36}]/SiO_2$	N/A	N/A	N/A	*In vitro*	2010	48
	$Na_9EuW_{10}O_{36}@$polymerized acrylic acid (PAA)	Mitochondria-targeting peptide	∼60 nm	50 μg mL^{-1}	*In vitro*	2015	49
CT	$(Et_2NH_2)_{10}[Zr(PW_{11}O_{39})_2]$	N/A	N/A	35 mg mL^{-1} PBS	*In vivo*	2019	62
	$K_{16}[Hf(\alpha_2\text{-}P_2W_{17}O_{61})_2]$	N/A	N/A	35 mg mL^{-1} PBS	*In vivo*	2018	63
	$GdW_{10}@BSA@Ti_3C_2$	N/A	∼309 nm	20 mg kg^{-1} body weight	*In vivo*	2018	64
	BSA-coated $Na_9[GdW_{10}O_{36}]$	N/A	∼3.5 nm	75 μmol kg^{-1} body weight	*In vivo*	2016	83

POMs are intrinsic contrast agents in CT imaging as many of them contain high atomic number elements (such as Hf, Zr and W) to attenuate the X-ray intensity as illustrated in Table 2.[62–64] As a result, some paramagnetic POMs can be used in both CT and MRI based on their unique composition to achieve multi-functional imaging information on diseases. GdW_{10}-based POM complexes were reported to serve as such a bifunctional imaging contrast agent, in which Gd dealt with T_1-weighted MR imaging and W with high atomic number ($Z = 74$) contributed to CT imaging. Meanwhile, the stabilization of the POM by binding to bovine serum albumin (BSA) allowed the formed complex to have high biocompatibility for further clinical application. In detail, a 2D Ti_3C_2 MXene material that was modified with PEG groups on its surface was adopted to collect the BSA covered GdW_{10} cluster. After the intravenous injection of the BSA-GdW_{10}/PEG-Ti_3C_2 composite nanosheets, MR images that were recorded at different time points clearly demonstrated the continuous enhancement of T_1-weighted MRI signals. The imaging revealed the gradual accumulation of GdW_{10} in the tumor region of 4T1 tumor-bearing mice *via* the enhanced permeability and retention (EPR) effect. Correspondingly, the CT signal at the tumor site was observed after the intra-tumoral (i.t.) administration of composite nanosheets, as shown in Fig. 4. These results not only confirmed the practicability of POMs for bimodal imaging, but also pointed out a doubly functional theranostic nanoplatform.[64] Additional examples of collected MRI and CT performance figured out that GdW_{10} was a promising candidate for more dual-mode real-time imaging. When the imaging characteristics of POMs are combined with other imaging modalities, more multifunctional imaging techniques can be achieved.[65] The feature of imaging allows diagnostic-imaging guidance and, in conjunction with treatment, tumor therapy under imaging monitoring can also be realized.

3. The photothermal properties of POMs

The general method of PTT is to drive photosensitizers concentrated in the tumor position to generate heat for the ablation of tumor cells. The heat derived from the transduction of irradiation light in the picosecond time domain due to electron–phonon and phonon–phonon processes sharply increases the local temperature in a short period of time.[66] The light source and
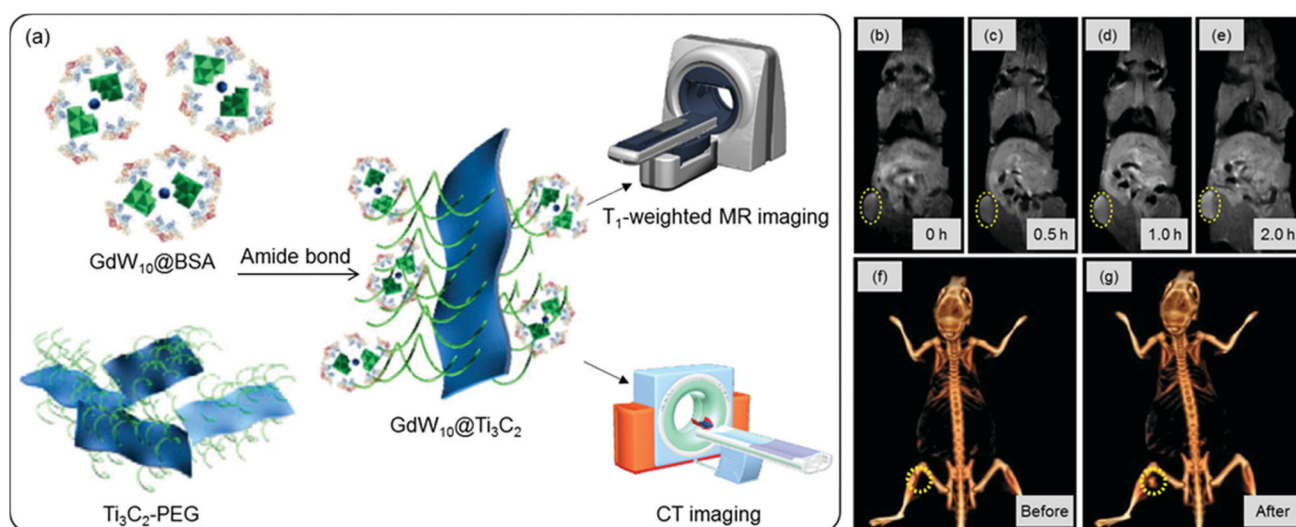

Fig. 4 (a) Schematic illustration of the synthesis of $GdW_{10}@Ti_3C_2$ composite nanosheets, and *in vivo* T_1-weighted MRI results at tumor and liver positions of 4T1 tumor-bearing mice after i.v. administration of $GdW_{10}@Ti_3C_2$ at (b) 0 h, (c) 0.5 h, (d) 1.0 h and (e) 2.0 h. The *in vivo* 3D reconstruction from CT images of 4T1 tumor-bearing mice is shown in (f) before and (g) after the i.t. injection of $GdW_{10}@Ti_3C_2$ composite nanosheets. Reprinted with permission from ref. 64. Copyright 2018, Springer Nature.

photosensitizers together determine the effect of PTT. In the PTT process, high light intensity leads to necrosis due to the higher local temperature, while suitable irradiation intensity only promotes apoptosis, as the heat causes irreversible damage to cancer cell membranes and initiates protein denaturation.[67,68] Especially, cancer cells have a lower ability to endure elevated heat than normal cells, owing to microstructure defects caused by rapid proliferation.[69,70] To ensure light efficiency for phototransduction and reduce the damage to normal tissue, the laser used is mainly NIR light as the skin absorption coefficient values in this region are the lowest. No matter what kind of material is employed, the photosensitizers used in biological systems need to possess three significant features: (1) good biocompatibility, (2) a strong ability to absorb NIR light, and (3) high photothermal conversion efficiency. The photothermal conversion efficiency is usually evaluated by recording transient temperature changes during heating and cooling in an experiment in line with the laser power and the concentration of photosensitizers in the media.[71] Following Roper's and Hu's reports,[72,73] in the calculation of the photothermal conversion efficiency, the total energy of the system is conserved, which can be expressed by eqn (1), where Q_{NP} and Q_{Dis} refer to light energy absorbed by nanoparticles and the container, and Q_{Surr} represents environmental energy dissipation. The photothermal conversion efficiency η can be calculated using the following eqn (2), where T_{Max} and T_{Surr} refer to the equilibrium temperature and the surrounding temperature, I refers to the incident light power, A_λ represents the absorption at this wavelength, h means the coefficient of heat conduction, S represents the surface area of the container, and hS can be calculated by the cooling curve using eqn (3)–(5).

$$\sum_i m_i C_{pi} \frac{dT}{dt} = Q_{NP} + Q_{Dis} - Q_{Surr} \qquad (1)$$

$$\eta = \frac{hS(T_{Max} - T_{Surr}) - Q_{Dis}}{I(1 - 10^{-A_\lambda})} \qquad (2)$$

$$hS = \frac{\sum_i m_i C_{pi}}{\tau_s} \qquad (3)$$

$$\tau_s = -\frac{t}{\ln \theta} \qquad (4)$$

$$\theta = \frac{T - T_{Surr}}{T_{Max} - T_{Surr}} \qquad (5)$$

Except for the commonly used photosensitizers, POMs as a kind of polyanion inorganic clusters have attracted much attention by reason of their ability to be easily oxidized and reduced with no structural change. POMs are composed of transition metals bridged by oxygen atoms, and the metals in most POMs are in their highest oxidation state. Some metals are reduced to lower states when POMs are reduced, and these reduced POMs with mixed valent metal ions can retain the original structures of their oxidized parents and display a dark blue color, which are called heteropoly blue. With the reduction of POMs, the intensity of the charge transfer band in the UV region decreases, and a new intervalence charge transfer (IVCT) band appears in the long wavelength region. The intensity and position of the IVCT band of heteropoly blue can be affected by the degree of reduction.[74] For some heteropoly blues, the existence of IVCT brings out the NIR absorption bands, and the band intensity increases as the reduction degree deepens. The existence of ground-state delocalization is the cause of the IVCT band. There are two main ways to delocalize electrons in heteropoly blue: (1) the jump of thermally activated electrons from one metal atom to the next; and (2) by bridging oxygen atoms to form a π bond, the electrons are delocalized from the ground state of the reduced metal atom to that of the adjacent one. Moreover, the degree of π interaction is related to the angle M^{5+}–O–M^{6+}, and ground-state delocalization is favored as the angle approaches 180°.[75] Thus, heat-activated electron hopping is more likely to happen. When the excited electron returns to the ground state, the energy dissipation takes various forms. Similar to the production of fluorescence, which has been described above, the nonradiative relaxation processes produce a photothermal conversion effect.[76] That is why near-infrared light with single photons of low energy can still stimulate some POMs for photothermal conversion.

POMs in the heteropoly blue state possessing strong NIR absorption exhibit photothermal properties because of the existence of reduced atoms (mainly Mo^V, W^V, and V^{IV}).[77–79] The acquisition of POMs in the heteropoly blue state mainly depends on the reduction method, direct synthesis and hydrothermal synthesis. Except for some macronuclear molybdenum clusters crystallizing in the heteropoly blue state,[80,81] Xu et al. developed a "directed precursor self-assembly" strategy for the facile synthesis of heteropoly blues.[82] Hydrothermal synthesis is also an important way to prepare solid compounds with special structure and functional properties. The reduction method has the ability to convert POMs into heteropoly blue, which mainly includes electrochemical reduction, photochemical reduction and reductant reduction. Due to the unique structure and abundant composition, many heteroatoms, including Gd, Mn, Eu and so on, can be incorporated into the POM framework to enrich the properties. Zhao et al. synthesized BSA-coated GdW_{10} nanoclusters; after electrochemical reduction, the resulting dark blue GdW_{10}@BSA nanoclusters showed strong absorbance at around 800 nm, which was attributed to the IVCT between W^{VI} and reduced W^V, to enable the nanoclusters to function as photothermal absorbing agents to convert NIR optical energy to thermal energy.[83] But the apparent negative factors are the introduction of external sensitizers, which may result in unwanted side-effects. Only by realizing targeted delivery and reducing the concentration of photosensitizers in normal tissue can the by-effect of molecular invasion be reduced to the lowest extent. As some POMs easily gain and lose electrons,[84] the overexpressed reductive glutathione (GSH) in the tumor microenvironment (TME) can transform Mo-based POMs without photothermal properties to heteropoly blues. As a result, the POMs perform as a photosensitizer specific to the tumor and the passive targeting property endows them with enhanced effectiveness.

This journal is © The Royal Society of Chemistry 2020

J. Mater. Chem. B, 2020, 8, 8189–8206 | 8195

4. Various PTTs of POMs

4.1 PTT at NIR-I

4.1.1 Bare clusters for PTT at NIR-I. Though tumor cells are less resistant to high temperature in comparison to normal cells and tissues, it is very hard to control the photothermal effect to reach the level that only cancer cells are killed at the present stage, especially in the case where the disease positions are very small or unconfirmed. As a result, photosensitizers are always designed to be targeting so that the hurt to the surrounding healthy tissues can be extremely minimized. The NIR-I photothermal therapy of POMs in the reduced state has been studied over recent years. Except the excellent photothermal conversion efficiency, naked POMs were used as passive targeting agents even if their sensitivity to the TME was considered. The main reason is that there is no special binding group on the cluster surface for all the interactions with biomolecules are non-special and electrostatic interaction is the main force. Thus, the passive targeting of photothermal POMs is mainly sourced from the enhanced EPR effect due to the responsiveness of the TME. The concentration of nanomaterials in the tumor region largely depends on the size, shape and surface charge of the nanoparticles.[85] Usually, nanoparticles with small diameters less than 5.5 nm resulted in rapid and efficient urinary excretion and elimination.[86] To achieve longer circulation, nanoparticles with a diameter between 30 nm and 200 nm are often indispensable.[87] Especially, the increased size (100–200 nm) makes these nanoparticles accumulate in the tumor position more efficiently through the EPR effect, despite the smaller nanoparticles exhibiting better

penetration depth.[85] Therefore, an effective strategy for small nanoparticles is to design a "small–big" photothermal agent, which can stay as small molecules during circulation in the bloodstream and then self-assemble into big aggregates in tumors under activation by the TME to strengthen the EPR effect.

As an example, the aggregation of Mo-based POM clusters was modulated to obtain large but well dispersed assemblies in the acidic tumor environment due to the decreased local pH.[88] A Keggin-type POM was synthesized by a facile one-pot approach using $(NH_4)_6Mo_7O_{24}·4H_2O$ and $NaH_2PO_4·12H_2O$. As shown in Fig. 5, the suitable acidic environment in tumor cells was favourable for the POM clusters to combine with protons. The reduced surface charge in the acidic state is believed to promote self-assembly due to the re-balanced interaction decreasing the electrostatic repulsion between these clusters. As a result, the assembled POMs at about a hundred nanometers possessed an enhanced EPR effect, which allowed the POMs to generate passive targeting. Thus, the aggregation in the acidic tumor environment not only increased the concentration of POMs in the tumor position, but also enhanced the near-infrared absorption and the migration of the absorption peak in response to the reducing ability in the TME caused by the IVCT between Mo(v) and Mo(vi) through bridged oxygen atoms. With different pH and successive reductions, the photothermal effect presents a dependency in terms of the corresponding acidity- and reducing ability-dependent absorbance at 808 nm. Due to the hypoxia and reductive environment of the tumor region compared to normal tissue,[89,90] the photothermal conversion efficiency of POMs was greatly improved. The transformation of the electronic structure
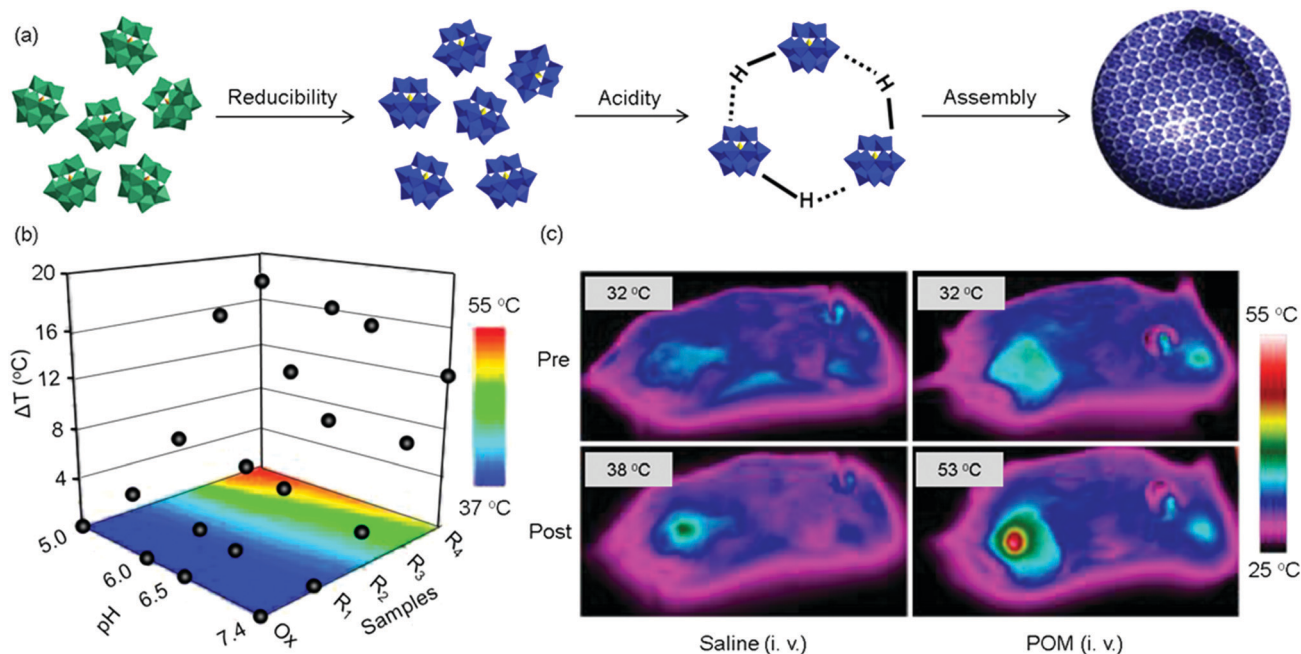

Fig. 5 (a) Schematic diagram proposed for low-pH-induced self-assembly of reduced POM clusters into an aggregated structure, (b) acidity- and reducing ability-dependent temperature increase under NIR irradiation at 808 nm, and (c) PTI of the representative thermal response in 4T1 tumor-bearing mice 1 h after intravenous injection with saline or POM. Reprinted with permission from ref. 88. Copyright 2016, American Chemical Society.

8196 | J. Mater. Chem. B, 2020, 8, 8189–8206

This journal is © The Royal Society of Chemistry 2020

in response to the stimulation of the TME brings in different photothermal conversion efficiency of POM clusters between the agents inside and outside the tumor, which causes minimal damage to the surrounding normal tissues owing to the killing effect of hyperthermia.[88] The sensitivity and unique response of POMs are apparently conducive for realizing tumor-specific photo-hyperthermia. However, such examples are pretty fortunate because for common clusters, the assembly of them *versus* the acidity range in tumor cells are difficult to meet the required pH windows for possessing narrow range of pH stability. On the other hand, it is inevitable that the naked clusters bind with proteins and other biomolecules as reported in some publications, which may induce cell toxicity.[17,91] In addition, the dissociation of naked POMs in human tissues seemed also unavoidable during metabolism. Hence, suitable protection on the POM surface becomes necessary while the covering layer makes the POM cluster assembly easier so that the targeting behaviour becomes no longer dependent on the local acidic environment.

4.1.2 POM complexes for PTT at NIR-I. In order to reduce the biotoxicity while enhancing the structural stability and ensure the photothermal conversion efficiency, the strategy adopted was to enwrap POMs with positively charged biocompatible molecules, such as peptides,[92] proteins,[93] mesoporous silica (MSN),[94] cationic surfactants,[95] and polymers,[96] through electrostatic interactions. The formed ionic complexes demonstrated series features performing the role of photosensitizers in the following aspects: (1) enhanced biocompatibility and structure stability of POMs during the circulation process; (2) a possible modification site of target groups; (3) a position for loading drugs and other sensing groups; and (4) synergistic functions. Besides BSA, a food-borne antioxidant peptide, soybean pentapeptide,[97] was reported to combine with photothermal POMs (r-$H_3PMo_{12}O_{40}$) to increase the clusters' stability and biocompatibility for PTT. In another important study, as shown in Fig. 6,[98] by coating a giant ring-like molybdenum blue cluster $Na_{15}[Mo^{VI}_{126}Mo^{V}_{28}O_{462}H_{14}(H_2O)_{70}]$ (abbrev. as Mo_{154}) with photothermal properties with a biocompatible cationic dendron bearing triethylene glycol (TEG) monomethyl ether terminal groups through electrostatic interactions, the formed core–shell supramolecular composite exhibited mono-dispersion and low cytotoxicity on account of its uniform size, precise chemical composition and definite molecular weight. The stability of the POMs was greatly improved by the presence of a dense hydrophobic layer on the surface of POM clusters, while the photothermal conversion effect was well retained after cationic surfactant coating.

Importantly, the surface covering surfactant component constructed space to load drugs and other functional guest molecules.[65,99] The delivered drug DOX was released together with the PTT process, and double therapeutic effects can be obtained. Of course, the enrichment of the drug-loaded POM composite at the tumor position was carried out by PTI identification in the course of PTT.

4.1.3 Synergistic systems for PTT at NIR-I. Definitely, besides the surface stability and biocompatibility, suitable surface modification of surface covered POM complexes improved the whole performance during PTT. Although the chemical composition and structure are still not clear, an *in situ* prepared reduced phosphate/tungstate nanocomposite protected by gallic acid while serving as a reductant displayed a non-inflammatory photothermal cancer therapy property, which was normally inevitable during PTT.[100] In a more complicated system, the photothermal effect of POMs was used for the treatment of Alzheimer's disease. Reduced POMs with Keggin, Wells–Dawson, and Anderson–Evans structure were smartly embedded in the pores of MSNs. To ensure no leakage occurrence before it was allowed, the cluster loaded MSNs were further incorporated into a thermally sensitive polymer, poly(N-isopropylacrylamide-co-acrylamide), by forming a three-component nanocomposite within about 200 nm in diameter. It should be mentioned that in all cases, the simple enwrapping of the POMs does not restrict the photothermal effect by remote light radiation. On one hand, upon exposure to 808 nm light, photothermal transduction facilitates the disaggregation of the preformed Aβ fibrils at a controlled temperature. On the other hand, external polymer responses to the temperature increase allowed the POMs to be released from the composite and the exposed cluster restricted the aggregation of Aβ monomers through binding the protein. In addition, the path to form Aβ fibrils can be blocked by exhausting the reactive oxygen species (ROS), and the oxidized POM still possess the capability of inhibiting the fibrilization of Aβ monomers. Interestingly, among the used POMs, Wells–Dawson type POMs demonstrated much better behaviour.[101]

4.2 PTT at NIR-II

In contrast to NIR-I, PTT at NIR-II bearing a longer wavelength is even more practical because of its deep tissue penetration and higher maximum permissible exposure (MPE, 1 W cm^{-2} for 1064 nm, while it is 0.33 W cm^{-2} for 808 nm and 0.72 W cm^{-2} for 980 nm, American National Standard for safe use of Lasers, ANSI Z136.1-2007).[38,102,103] The application of 980 nm is limited as the
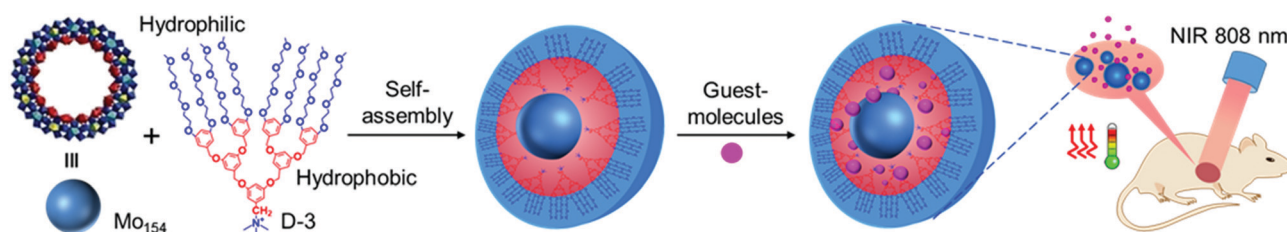

Fig. 6 Structural illustration of the preparation of $D_{15}Mo_{154}$ complex micelles, and the drug molecule loading and photothermal controlled release locally upon laser irradiation. Reprinted with permission from ref. 98. Copyright 2018, Royal Society of Chemistry.

absorbance of water becomes strong at this wavelength, which causes damage to normal tissues.[104] Thus, a still longer wavelength is demonstrated to be more useful in potential applications. In comparison to the widely used materials exhibiting PTT properties at NIR-I, the materials displaying an NIR-II photothermal effect are pretty few. But a few overview articles summarized the comprehensive performance at NIR-II in very recent years.[105,106] Fortunately, in the POM family, some POMs, such as Mo_{154}, show strong absorption at around 1080 nm,[107] which we call the NIR-II bio-window now, but their photothermal properties in this region were rarely studied. Most recently, Dong and his co-workers synthesized a Mo_2C-derived POM by one-pot oxidation of β-Mo_2C in aqueous dispersion using H_2O_2 as the oxidant, as shown in Fig. 7.[108] Strictly, the prepared product should not correspond to the real meaning of POM due to the unknown cluster structure and chemical composition. However, the properties of the obtained composite are very similar to those of the molybdenum cluster used in NIR-I PTT discussed above. The reported examples showed similar responsiveness to the TME, resulting in the enhanced EPR effect and passive targeting at NIR-II. The Mo_2C derived POM can be converted between oxidized and reduced states when stimulated by the over-expressed H_2O_2 and GSH in the tumor environment. The H_2O_2 over-expressed in tumor sites can be converted into more toxic ROS by the Mo_2C derived POM for chemo-dynamic therapy. The reduced POM shows broad absorption in the NIR-II bio-window and the intensity was believed to be affected by the self-assembly of POMs in the acidic environment. Besides the deep tissue penetration,

the photothermal conversion efficiency of the cluster in the NIR-II bio-window reached 47.8%, which was higher than those of many reported photosensitizers in this region. Some other Mo-based POMs were also demonstrated to be applicable as NIR-II PTT agents with high photothermal conversion efficiency after reduction.[109] These unique properties of POMs (Table 3) encourage further investigation to realize the photothermal related biomedical applicability of real POM clusters with precise chemical structures and chemical compositions.

5. PAI of POMs

5.1 Basis of PAI

The ultrasound detection technique tracks active organisms by the principle that acoustic wave contrast occurs between two tissues with different acoustic impedance during the sound crossing the reflecting interface, in comparison to the fact that the CT and MRI methods only provide information on a static tissue position. The specialties of US imaging lie in its high spatial and temporal resolution and clinical translation. PAI, known as optoacoustic imaging, based on the detection of light-induced US waves, provides a new choice to raise the quality of ultrasound imaging with high resolution. Under nanosecond pulsed or temporally modulated light illumination, specific endogenous tissue chromophores or exogenous contrast agents absorb and convert optical energy to a rapid rise of temperature at a local position, resulting in the generation of US waves.[110,111]
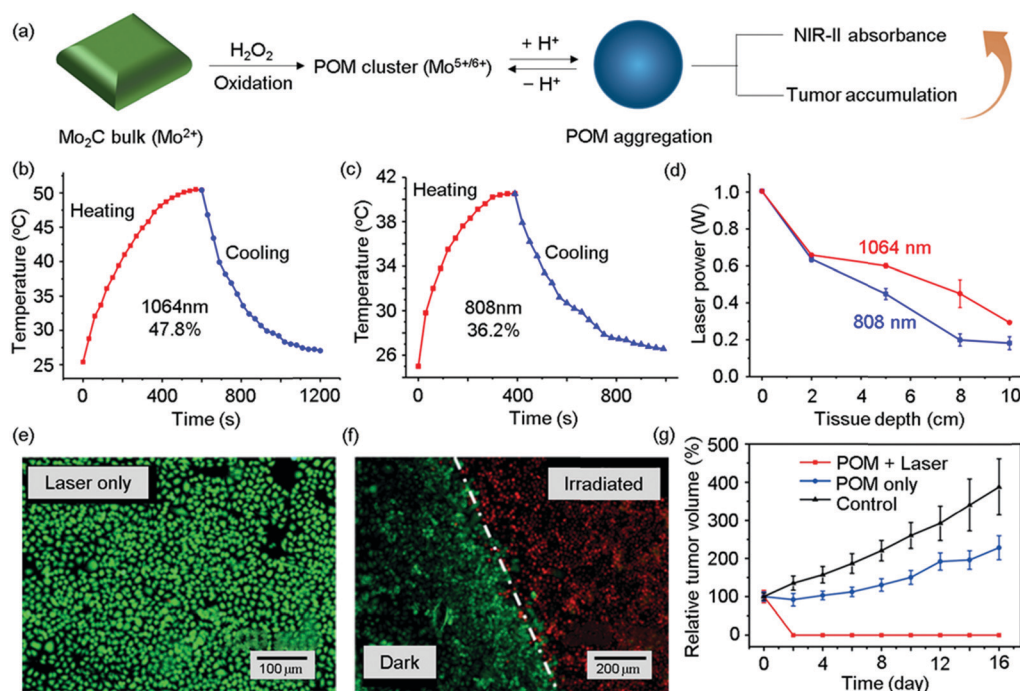

Fig. 7 (a) Schematic illustration of the preparation of reduced POM clusters and their low-pH-induced self-assembly, photothermal conversion efficiency of the reduced POM clusters under laser light at (b) 1064 nm and (c) 808 nm, and (d) corresponding plots of the tissue penetration ability at the two wavelengths. (e and f) Luminescence images of calcein-AM/PI double staining of HeLa cells with different treatments, and (g) plots of tumor volume over time after treatment. Reprinted with permission from ref. 108. Copyright 2019, John Wiley & Sons.

8198 | *J. Mater. Chem. B*, 2020, **8**, 8189–8206

This journal is © The Royal Society of Chemistry 2020

Table 3 The summary of POMs and their composites acting as a multifunctional platforms for combined PTT and other therapy methods

POMs/POM composites	PTT laser@laser power	Size	Condition	Therapy	Imaging	Time	Ref.
BSA-coated $Na_9[GdW_{10}O_{36}]$	808 nm 1.0 W cm^{-2}	$\approx$3.5 nm	In vivo	PTT@radiotherapy	MRI/CT	2016	83
Mo-POM	808 nm 1.5 W cm^{-2}	1 nm (pH 7.4)	In vivo	PTT	PAI/PTI	2016	88
rPMo$_{12}$-soybean pentapeptide Ser-His-Cys-Met-Asn	808 nm 1.0 W cm^{-2}	60 $\pm$ 15.4 nm	In vitro	Photothermal antibacterial	PTI	2019	97
Mo$_{154}$@dendritic cation (D-3)	808 nm 1.0 W cm^{-2}	7.5 $\pm$ 2.2 nm	In vivo	Chemo-PTT	PTI	2018	98
W-POM nanocluster	808 nm 1.5 W cm^{-2}	2.0 $\pm$ 0.1 nm	In vivo	Non-inflammatory PTT	PTI	2020	100
rPOM@MSN@copolymer	808 nm 1.8 W cm^{-2}	186.4 nm	In vitro	PTT of Alzheimer's disease	N/A	2018	101
Mo$_2$C-derived POM	1060 nm 0.8 W cm^{-2}	<10 nm (pH 7.4)	In vivo	NIR-II PTT@chemodynamic	NIR-II PAI/PTI	2019	108
Fe-doped POM	1060 nm 1.0 W cm^{-2}	12.9 nm (pH 7.4)	In vivo	NIR-II PTT@chemodynamic	PAI/PTI	2020	109
Ox-POM	808 nm 1.5 W cm^{-2}	1.9 nm (pH 7.4)	In vivo	PTT	PAI/PTI/PET	2017	116
Semiconducting polymer brush@POM	808 nm 0.5 W cm^{-2}	$\approx$100 nm (pH 7.4)	In vivo	Enhanced PTT	PET/PTI	2018	117
UCNP@mSiO$_2$-POM-DOX	808 nm 0.72 W cm^{-2}	68.3 nm	In vivo	Chemo-PTT	CT/UCL/MRI/PTI	2018	125
UCNP@mSiO$_2$-POM-DOX@PEG	808 nm 0.72 W cm^{-2}	65.8 nm	In vivo	Chemo-PTT	CT/UCL/MRI/PTI	2018	126
UCNP@mSiO$_2$-POM-DOX@FA-HA	808 nm 0.72 W cm^{-2}	120 nm	In vivo	Chemo-PTT	CT/UCL/PTI	2019	127
HMON-PEG/POM@Mn$_2$(CO)$_{10}$	808 nm 1.0 W cm^{-2}	124.7 $\pm$ 13.7 nm	In vivo	PTT-enhanced gas therapy	PAI/PTI/PET	2018	130

The generated photoacoustic signal, which carries information on the light absorption characteristics of the tissue chromophores or contrast agents, can be used to reconstruct the image of the light absorption distribution in the tissue. PAI combines the advantages of ultrasound and optical imaging with high spatial resolution, and has promise for guiding surgical and interventional procedures because of the provided molecular information on tissue with high spatial resolution in real-time.[112]

However, there are still two crucial factors during the further development of PAI, one is the selection of the wavelength to be used as the radiation light source and the other is the utilization of contrast agents serving as photosensitizers. Again, to enhance the tissue permeation, pulsed NIR laser light becomes preferable and a longer wavelength is necessary for practical measurement due to its deeper penetration. In addition, the local fast photothermal effect is also one of the decisive conditions for getting high-resolution imaging.[113] Based on these requirements, the high-quality photothermal materials match such prerequisite conditions in utmost to the PAI and the POMs become the premium cluster candidates for the combined detection technique suitable for active organisms.

5.2 Tumor detection

POMs in the reduced state are not as stable as those in the fully oxidized state, especially when they are exposed in the air. In addition, to exclude background noise, a large difference between the position to be detected and other places benefits the imaging quality. Therefore, after injection into living tissue and undergoing internal retention, the change of their state has to be considered carefully. On the other hand, the oxidation state can be modulated with regard to the environment in which POMs are located. In pioneering work,[114] a POM sourced from $(NH_4)_6Mo_7O_{24}\cdot 4H_2O$ was used to combine with a typical dye croconaine (CR), forming a nanocomposite with a size ca. 100 nm through electrostatic and hydrogen bond interactions. Adjusting the pH allowed the nanocomposite monomer to aggregate into a larger one with a diameter over 1000 nm. During the in vivo retention, the nanocomposite in the fully oxidized state can be delivered and then enriched at the tumor position. GSH serving as an important reducing species is involved in a variety of cellular functions in vivo. An imbalance of GSH means the occurrence of bodily diseases, and particularly the overexpression of GSH is proved to be a typical hallmark of tumors.[90] Thus, the passively targeted POM in the composite aggregates can be reduced to the state with partial Mo(v) and the cluster starts to show NIR absorption due to the IVCT transition. With this mechanism, the over-expressed GSH can be quantified precisely via the PAI process for the early diagnosis of GSH-related deep-seated diseases while confirming the cancer position and later prompt treatment (Fig. 8). Such a result was supported by the PAI of co-assembled CR molecules in the composite aggregate, by reasons of its intrinsic NIR absorption at 700 nm. The contrast of both signals from Mo based POM clusters in the reduced state with NIR absorption at 866 nm and the CR molecule quantifies the distinct GSH concentration change by detection of the absorbance values. Spontaneously, the PA signal ratio of them at the two wavelengths (PA$_{866}$/PA$_{700}$) shows a much higher value than most existing ratiometric PAI probes on account of the opposite NIR absorbance change in response to GSH.

5.3 PAI-guided PTT

POMs possess native features to accomplish multi-function integration because of their structural and physicochemical properties. In addition to the combination with CT and MR imaging, in situ PA imaging is also a smart route for multi-modal imaging-guided PTT. With the assistance of contrast agents or photosensitizers, the PTT process can be monitored by PAI and PTI during the therapeutic process.[115] As described, PTT is naturally accompanied by PTI for providing real-time temperature changes recorded by the thermal imager, and the effects of different photothermal reagents can be visually seen in vitro and in vivo. In contrast, PAI can precisely position the
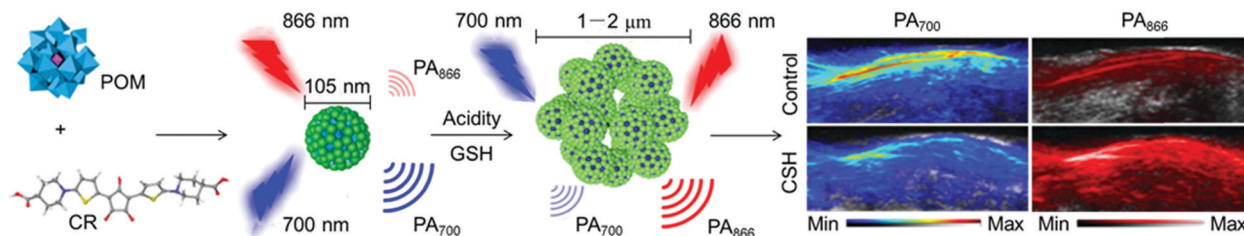
Fig. 8 Schematic illustration of the CR-POM nanosphere and its assembly for specific ratiometric PAI for intratumoral GSH. Reprinted with permission from ref. 114. Copyright 2019, American Chemical Society.

tumor and guide the PTT process as PAI can track the tumor uptake of the photosensitizer at different moments, or the content of effective photosensitizer in the TME. The basic principle of PAI makes it non-exclusive to the parallel PTT activity at the same position. A full study of bio-responsive POM clusters for redox-activated PAI-guided PTT for 4T1 tumors demonstrated such a combination. When the as-prepared molybdenum-based POM cluster (denoted as Ox-POM), prepared from the reaction of $(NH_4)_6Mo_7O_{24}\cdot4H_2O$ and $NaH_2PO_4\cdot12H_2O$ at room temperature, was intravenously injected into mice, its pH sensitivity to the TME during internal retention causes the cluster to be acidified, yielding aggregates. Meanwhile, the over expressed GSH in tumor cells reduced the cluster to the heteropoly blue state, allowing the production of NIR absorption and the photothermal effect under the radiation of a laser. *In vivo* redox-activated PAI on 4T1-tumor bearing mice at different times was conducted. The observed PA signal revealed the effective accumulation of reduced heteropoly blue in the tumor area. The gradually increased intensity from 1 to 6 h showed clear tumor tissue penetration and the highest concentration of reduced heteropoly blue at the sixth hour provided the most appropriate time for PTT. The maintained PA signal at an extended time of 24 h was observed to detect the

enhanced EPR effect induced by the assembly of clusters in the tumor tissue. The time-varying temperature change caused by the laser irradiation can be captured by photothermal imaging to judge whether it is sufficient to thermally ablate the tumor (Fig. 9).[116] A strong and powerful combination can be achieved when the Mo-based POM clusters are combined with other photosensitizers for stronger PAI guided PTT. A paradigm based on semiconducting polymer brushes and Mo-based POM clusters (SPB@POM) is rationally designed for enhanced tumor-specific phototheranostics. The integration of the intrinsic photothermal properties sourced from organic semiconductor polymers and inorganic POMs induced by the TME resulted in improved PAI contrast and enhanced PTT efficacy.[117] The *in vitro* and *in vivo* experimental results have confirmed the synergistic effect. PAI guided PTT represented an important breakthrough in realizing the functional integration of POMs.

6. POM based multi-functional imaging and treatment systems

Multi-functional theranostic nanocomposites pursuing more accurate imaging and therapy have been studied widely in
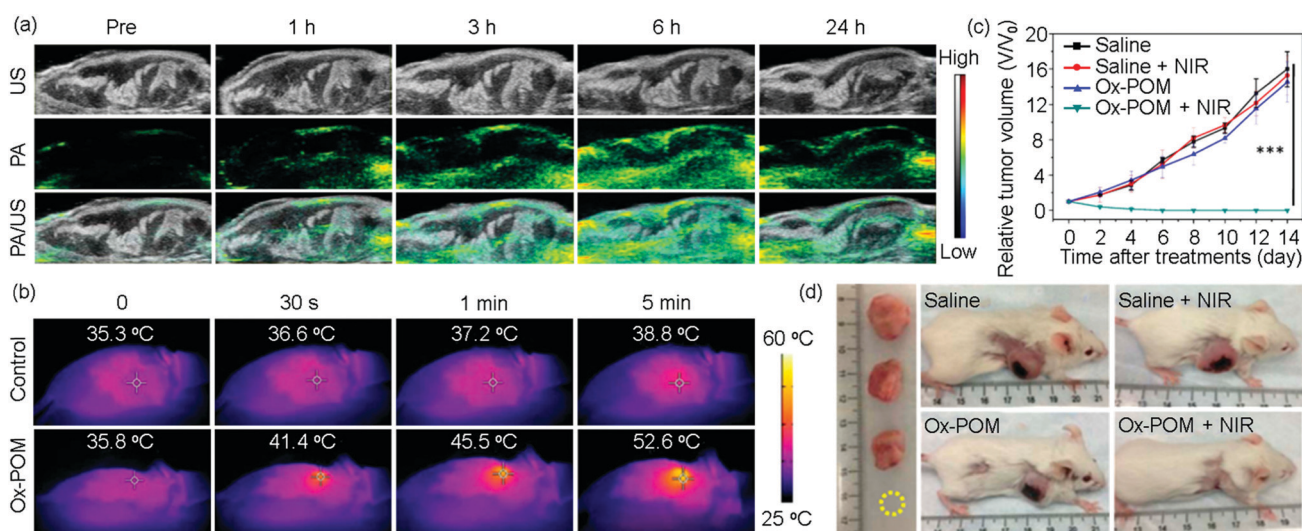

Fig. 9 (a) *In vivo* PA images of 4T1 tumor-bearing mice before and after intravenous injection of Ox-POM clusters until 24 h. (b) Photothermal images of 4T1 tumor-bearing mice before and after intravenous injection of Ox-POM clusters under continuous 808 nm laser irradiation within different durations. (c) Tumor volume changes and (d) profiles of 4T1 tumors as well as photographs of mice after each treatment at 14 days post treatment. Reprinted with permission from ref. 116. Copyright 2019, American Chemical Society.

8200 | *J. Mater. Chem. B*, 2020, **8**, 8189–8206

This journal is © The Royal Society of Chemistry 2020

recent years. The fully developed nanotechnology and nano-materials provide almost all required strategies and detailed procedures for the preparation of nanocomposite materials as multi-function sensitizers and probes. On the other hand, the monotony PTT is not always satisfied on account of the heterogeneous distribution of resulting heat,[118] and combination with other methods such as chemotherapy and gas therapy becomes necessary to accomplish exhaustive killing of tumor tissues.

6.1 Combination of PTT and chemotherapy

The pleiotropic effects of hyperthermia are in favour of its extended application with chemotherapy.[119] Many positive results from random experiments with regard to POM-based materials have established hyperthermia in combination with chemotherapy as a novel clinical modality for the treatment of cancer. Preclinical studies have confirmed that such synergistic effects are considerably significant because the thermal enhancement of drug cytotoxicity is accompanied by thorough cellular death and necrosis, decreasing the possibility of oncogenic potential.[120] The additional advantage of the combination is that hyperthermia can be used for the controlled release of drugs by targeting a region of chemotherapy limited to the heated tumour. While considering the merits of PTT of low toxicity, easy tunability and high spatiotemporal resolution,[121] the depth-dependent decline of the laser intensity and heat shock response[122,123] can be partially overcome during combined chemotherapy because less hyperthermia (normally at 39–42 °C) is required during combination with other therapies.[124] Considering that POMs still do not show notable tumor therapeutic activity at the present stage, the adopted strategies for multi-clinic modality are to introduce additional drug molecules. There are two approaches to combine drug molecules with POMs, one is to form composites by adsorbing drugs bearing counter charges onto the cluster surface through electrostatic interactions, and the other is to incorporate them into the inner part of POM composites with inorganic/organic molecules, and/or polymers through various interactions. The former route is convenient and no extra component is introduced into the therapeutic system, which reduces the possibility of additional damage to the healthy organism. In contrast, the latter route can improve the non-specific release and the poor solubility of drugs, which still largely restrict their clinical performance. Thus, while conducting the role of PTT, POM-cored composites become promising candidates for drug carriers to carry out the controlled targeted release of drugs at the same time, realizing integrated chemotherapy in one system.

In a typical example which was introduced earlier, a giant wheel-like polyoxomolybdate cluster Mo_{154} was co-assembled with a cationic surfactant by ionic interactions to construct a stable complex with a precise chemical composition by forming a reverse micellar structure possessing a polyanionic POM core. The drug DOX in hydrochloride salt was then loaded in the hydrophobic area owing to the hydrophobic interaction, while the electronegativity of the POM supported the drug loading stability. Under the stimulation of NIR laser light,

the photothermal transduction-induced hyperthermia turns on the drug release and the shrinkage of the thermo-sensitive TEG block can also accelerate the process.[98]

In a more complicated inorganic porous system, $NaGdF_4$:Yb(Er)@$NaGdF_4$Nd(Yb) as a kind of up-conversion nano-particles (UCNPs) was covered by mesoporous silica through the hydrolysis reaction of tetraethylorthosilicate (TEOS), followed by grafting amino groups that can be protonated with 3-amino-propyltriethoxysilane. The produced pores with a diameter over 5 nm on the surface silica layer of nanoparticles together with the modified amino group under the neutral or acidic environment are good for the formation of polyanionic POM clusters via an in situ reaction of $(NH_4)_6Mo_7O_{24}\cdot4H_2O$ and NaH_2PO_4 in the presence of reductant L-ascorbic acid. With the reverse surface charge, the drug molecule DOX can be attached onto the hetero-poly blue cluster in the reduced state electrostatically. The intro-duced heavy elements allow the nano-composite to enhance CT imaging and the paramagnetic rare earth metal strengthens MRI largely. When NIR laser light at 808 nm was used, the upconver-sion of hybrid nanocomposite $NaGdF_4$:Yb(Er)@$NaGdF_4$Nd(Yb) caused luminescence with shorter wavelengths at 500–550 nm and 600–650 nm for luminescence imaging while the PTT of the reduced POM takes place at the tumor position at the same time, which triggers the on-site release of DOX, realizing combined chemotherapy.[125]

The improvement of the multiple platform system via the further surface modification of polyethyleneglycol on a superior upconversion nanocomposite $NaGdF_4$:Yb(Er)@$NaGdF_4$:Nd(Yb) demonstrated better biocompatibility. Meanwhile, Mn(II) was introduced during the composite synthesis to enhance the MRI and CT effects, while helps in the release of loaded drug molecules at inner-cell acidic conditions by breaking the Mn–O bond, as presented in Fig. 10.[126] In contrast to the passive targeting via the EPR effect, with the introduction of folic acid onto the surface of this type of nanocomposites with a $NaYF_4$:Yb(Er)@$NaYF_4$:Yb(Nd) core, combined PTT and chemo-therapy can be realized in tumor cells via an active targeting route.[127]

6.2 Combination of PTT and gas therapy

In addition to those typical model drug molecules that are embedded into nanocomposites beforehand and released under photothermal triggering at the needed moment, there are also other strategies in realizing controlled targeted chemotherapy, like low concentrations of carbon monoxide (CO) for gas therapy. As an emerging therapeutic approach, gas therapy utilizes toxic gases, such as nitric oxide (NO) and CO, to inhibit the activity of tumor cells.[128] Though a high concentration of CO causes great damage to the organism by affecting the ability to transport oxygen due to its binding to haemoglobin, low concentration CO can be used as a messenger molecule to regulate the physio-logical functions of the nervous system and immunity. CO at low concentration also shows significant potential for killing cancer cells by targeting mitochondria in tumor cells to increase their oxygen consumption, thus generating free radicals and eventually leading to the destruction of mitochondria.[129] The key point of gas

Fig. 10 (a) Schematic illustration of the synthesis of UCNC−DOX and DOX, and DOX loading and release along with NIR-modulated biodegradation, (b) photothermal images of U14 tumor-bearing mice before and after injection of UCNC−DOX upon 808 nm laser irradiation, (c) CLSM images of HeLa cells after various treatments, dyed with AM and PI, and (d) photographs of mice and relative tumor volumes. Reprinted with permission from ref. 126. Copyright 2018, Royal Society of Chemistry.

therapy is to ensure targeted delivery and controlled release so that the damage to normal tissues can be decreased to the minimum. Interestingly, the synergy from the PTT process becomes helpful to realize the targeted release of CO *via* photothermal stimulation.

As a typical example, as shown in Fig. 11,[130] sub-50 nm thioether/phenylene dual-hybridized hollow mesoporous organosilica nanoparticles (HMONs) with a hemolytic effect were constructed by an "ammonia-assisted hot water etching" method.
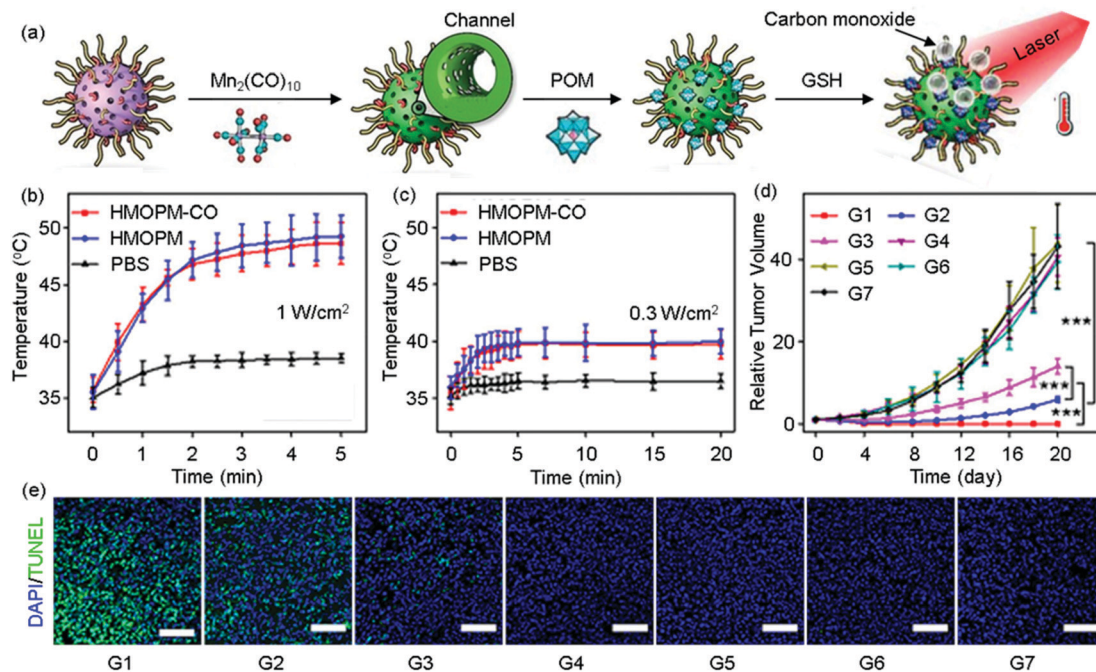

Fig. 11 (a) Schematic synthetic route of HMOPM-CO, *in situ* reduction and temperature rise-induced production of CO, temperature increase curves at tumor regions *versus* time during irradiation under a power of (b) 1.0 W cm^{-2} and (c) 0.3 W cm^{-2} in phosphate buffer saline (PBS), (d) tumor volume changes after post therapy with HMOPM-CO on a U87MG tumor model, and (e) corresponding fluorescence images of TUNEL assays on tumors acquired after 24 h of different treatments, where G1, HMOPM-CO + 1.0 W cm^{-2} (synergistic PTT/gas therapy); G2, HMOPM + 1.0 W cm^{-2} (PTT); G3, HMOPM-CO + 0.3 W cm^{-2} (gas therapy); G4, HMOPM + 0.3 W cm^{-2}; G5, HMOPM-CO; G6, +1.0 W cm^{-2}; G7, PBS. Reprinted with permission from ref. 130. Copyright 2018, American Chemical Society.

A typical gas-releasing molecule, $Mn_2(CO)_{10}$, was loaded through a hydrophobic–hydrophobic interaction, and Mo^{VI}-based POM clusters were modified on the surface of the nanoparticles. Thus, the POM-anchored nanocomposite possesses TME-responsive PA imaging contrast and enriches in the tumor site *via* the EPR effect. Accompanying the reduction of the POM cluster by GSH in inner tumor cells for performing PTT, the yielded NIR photothermal effect triggered the thermal decomposition of $Mn_2(CO)_{10}$, releasing a low concentration of CO. The synergistic PTT and gas therapy doubly accelerated the eventual cell apoptosis *via* a series of processes of accelerated biogenesis, mitochondria exhaustion, and elevated ROS production.

7. Conclusions and perspectives

From the above introduction, it is seen that during the search for diverse novel nanosized biocompatible materials targeting PTI and PTT, the POM family played an indispensable role due to its very broad structural and functional characteristics. In comparison to those established material systems, the cluster structures and chemical compositions of POMs have been well characterized. Meanwhile, the main physicochemical properties are deeply explored. The very small size (usually less than 5 nm) and high dispersion allow POMs to circulate *in vivo* while the surface charges make modification very convenient *via* a simple supramolecular approach for the construction of various nanocomposites to introduce other functional additives. Most importantly, the substitution of transition metal ions and the controllable modulation of the electronic structure endow POMs with more important sensitivity *versus* the local environment. At the present stage, we can see the strong capability of POMs as unique contrast agents in FL, MR, CT, NIR-related PAI and PTI, and combined imaging and PTT. POM cored nanocomposites as a multiple function platform can not only increase the cluster structure stability and long-term circulation and reduce the biotoxicity, but also have multimodal accurate diagnosis characteristics. The smart integration of POMs with inorganic, or organic/polymer materials leads to synergistic functions in active targeting, upconversion luminescence, chemotherapeutic effects and gas therapy for localized treatment of tumors.

While figuring out several profiles as a type of robust biomaterials, the full understanding of POMs in terms of the photothermal behaviour is in the burgeoning period and several challenges, such as understanding the detailed metabolism mechanism, finding out the possible metabolised products, carrying out the safety assessment of POMs, and so forth, are still under way. Even now, it is envisioned that the NIR-II photothermal specialty and responsiveness of POMs to the tumor microenvironment will open a new area for them in biomedical sciences, while it can be expected that POMs themselves will act as a potential drug carrier in the therapy of diseases under photothermally induced hyperthermia.

Conflicts of interest

There are no conflicts to declare.

Acknowledgements

Notes and references

1 G. S. Hong, J. T. Robinson, Y. J. Zhang, S. Diao, A. L. Antaris, Q. B. Wang and H. J. Dai, *Angew. Chem., Int. Ed.*, 2012, **51**, 9818–9821.
2 Z. H. Mei, D. Y. Gao, D. H. Hu, H. C. Zhou, T. Ma, L. Huang, X. Liu, R. Q. Zheng, H. R. Zheng, P. Zhao, J. Q. Zhou and Z. H. Sheng, *Biomaterials*, 2020, **251**, 120092.
3 A. Beda, A. R. Carvalho, N. C. Carvalho, S. Hammermüller, M. B. P. Amato, T. Muders, C. Gittel, K. Noreikat, H. Wrigge and A. W. Reske, *Crit. Care Med.*, 2017, **45**, 679–686.
4 W. H. Liao, P. Lei, J. B. Pan, C. Zhang, X. T. Sun, X. J. Zhang, C. S. Yu and S.-K. Sun, *Biomaterials*, 2019, **203**, 1–11.
5 F. Y. Li, Z. Y. Liang, J. N. Liu, J. H. Sun, X. Hu, M. Zhao, J. X. Liu, R. L. Bai, D. Kim, X. L. Sun, T. Hyeon and D. S. Ling, *Nano Lett.*, 2019, **19**, 4213–4220.
6 J. K. Willmann, N. van Bruggen, L. M. Dinkelborg and S. S. Gambhir, *Nat. Rev. Drug Discovery*, 2008, **7**, 591–607.
7 Y. R. Huang, S. He, W. P. Cao, K. Y. Cai and X.-J. Liang, *Nanoscale*, 2012, **4**, 6135–6149.
8 C. M. Pitsillides, E. K. Joe, X. B. Wei, R. R. Anderson and C. P. Lin, *Biophys. J.*, 2003, **84**, 4023–4032.
9 H. Y. Wang, J. J. Chang, M. W. Shi, W. Pan, N. Li and B. Tang, *Angew. Chem., Int. Ed.*, 2019, **58**, 1057–1061.
10 Z. J. Zhou, Y. Yan, L. Wang, Q. Zhang and Y. Y. Cheng, *Biomaterials*, 2019, **203**, 63–72.
11 L. Cheng, C. Wang, L. Z. Feng, K. Yang and Z. Liu, *Chem. Rev.*, 2014, **114**, 10869–10939.
12 J. J. Hu, Y. J. Cheng and X. Z. Zhang, *Nanoscale*, 2018, **10**, 22657–22672.
13 Y. J. Liu, P. Bhattarai, Z. F. Dai and X. Y. Chen, *Chem. Soc. Rev.*, 2019, **48**, 2053–2108.
14 T. Yamase, *Chem. Rev.*, 1998, **98**, 307–325.
15 B. Li, W. Li, H. L. Li and L. X. Wu, *Acc. Chem. Res.*, 2017, **50**, 1391–1399.
16 G. X. Wang, W. M. Guan, B. Li and L. X. Wu, *Curr. Opin. Colloid Interface Sci.*, 2018, **35**, 91–103.
17 N. Zhang, L. Y. Hong, A. F. Geng, J. H. Yan, S. Yao and Z. M. Zhang, *Chin. Chem. Lett.*, 2018, **29**, 1409–1412.

18 A. Bijelic, M. Aureliano and A. Rompel, *Angew. Chem., Int. Ed.*, 2019, **58**, 2980–2999.

19 Y. Y. Ma, L. Shi, M. C. Zhou, B. Li, Z. J. Chen and L. X. Wu, *Chem. Commun.*, 2019, **55**, 7001–7004.

20 G. Guedes, S. Q. Wang, H. A. Santos and F. L. Sousa, *Eur. J. Inorg. Chem.*, 2020, 2121–2132.

21 D.-E. Lee, H. Koo, I.-C. Sun, J. H. Ryu, K. Kim and I. C. Kwon, *Chem. Soc. Rev.*, 2012, **41**, 2656–2672.

22 R. Weissleder, *Nat. Rev. Cancer*, 2002, **2**, 11–18.

23 N. Lee, S. H. Choi and T. Hyeon, *Adv. Mater.*, 2013, **25**, 2641–2660.

24 F. Hyafil, J.-C. Cornily, J. E. Feig, R. Gordon, E. Vucic, V. Amirbekian, E. A. Fisher, V. Fuster, L. J. Feldman and Z. A. Fayad, *Nat. Med.*, 2007, **13**, 636–641.

25 X. Y. Zhong, X. W. Wang, G. T. Zhan, Y. A. Tang, Y. Z. Yao, Z. L. Dong, L. Q. Hou, H. Zhao, S. J. Zeng, J. Hu, L. Cheng and X. L. Yang, *Nano Lett.*, 2019, **19**, 8234–8244.

26 O. Rabin, J. Manuel Perez, J. Grimm, G. Wojtkiewicz and R. Weissleder, *Nat. Mater.*, 2006, **5**, 118–122.

27 B. Q. Zhou, L. F. Zheng, C. Peng, D. Li, J. C. Li, S. H. Wen, M. W. Shen, G. X. Zhang and X. Y. Shi, *ACS Appl. Mater. Interfaces*, 2014, **6**, 17190–17199.

28 S. Wang, H. Wang, C. Song, Z. C. Li, Z. J. Wang, H. Xu, W. J. Yu, C. Peng, M. Q. Li and Z. G. Chen, *Nanoscale*, 2019, **11**, 15326–15338.

29 Y.-K. Peng, S. C. E. Tsang and P.-T. Chou, *Mater. Today*, 2016, **19**, 336–348.

30 Y. Cao, L. J. Xu, Y. Kuang, D. S. Xiong and R. J. Pei, *J. Mater. Chem. B*, 2017, **5**, 3431–3461.

31 B. Wu, S.-T. Lu, H. Yu, R.-F. Liao, H. Li, B. V. Lucie Zafitatsimo, Y.-S. Li, Y. Zhang, X.-L. Zhu, H.-G. Liu, H.-B. Xu, S.-W. Huang and Z. Cheng, *Biomaterials*, 2018, **159**, 37–47.

32 B. H. Kim, N. Lee, H. Kim, K. An, Y. I. Park, Y. Choi, K. Shin, Y. Lee, S. G. Kwon, H. B. Na, J.-G. Park, T.-Y. Ahn, Y.-W. Kim, W. K. Moon, S. H. Choi and T. Hyeon, *J. Am. Chem. Soc.*, 2011, **133**, 12624–12631.

33 Y. Chen, D. L. Ye, M. Y. Wu, H. R. Chen, L. L. Zhang, J. L. Shi and L. Z. Wang, *Adv. Mater.*, 2014, **26**, 7019–7026.

34 K. K. Ng and G. Zheng, *Chem. Rev.*, 2015, **115**, 11012–11042.

35 A. Jablonski, *Nature*, 1933, **131**, 839–840.

36 L. Y. Zhao, Y. M. Liu, R. R. Xing and X. H. Yan, *Angew. Chem. Int. Ed.*, 2020, **59**, 3793–3801.

37 R. Weissleder and M. J. Pittet, *Nature*, 2008, **452**, 580–589.

38 A. N. Bashkatov, E. A. Genina, V. I. Kochubey and V. V. Tuchin, *J. Phys. D: Appl. Phys.*, 2005, **38**, 2543–2555.

39 A. M. Smith, M. C. Mancini and S. M. Nie, *Nat. Nanotechnol.*, 2009, **4**, 710–711.

40 G. C. Chen, Y. J. Zhang, C. Y. Li, D. H. Huang, Q. W. Wang and Q. B. Wang, *Adv. Healthcare Mater.*, 2018, **7**, 1800497.

41 Y. F. Tang, F. Pei, X. M. Lu, Q. L. Fan and W. Huang, *Adv. Opt. Mater.*, 2019, **7**, 1900917.

42 H. Wang, X. Y. Mu, J. Yang, Y. Y. Liang, X.-D. Zhang and D. Ming, *Coord. Chem. Rev.*, 2019, **380**, 550–571.

43 Y. J. Gong, F. Q. Bai, Z. D. Yu, Y. H. Bi, W. W. Xu and L. Yu, *RSC Adv.*, 2016, **6**, 8601–8604.

44 N. N. Lei, D. Z. Shen and X. Chen, *Soft Matter*, 2019, **15**, 399–407.

45 J. Zhang, Y. Liu, Y. Li, H. X. Zhao and X. H. Wan, *Angew. Chem., Int. Ed.*, 2012, **51**, 4598–4602.

46 J. Lu, Q. Kang, J. H. Xiao, T. Wang, M. Fang and L. Yu, *Carbohydr. Polym.*, 2018, **200**, 560–566.

47 Y. X. Guo, Y. J. Gong, L. B. Qi, Y. A. Gao and L. Yu, *J. Colloid Interface Sci.*, 2017, **485**, 280–287.

48 Y. Y. Zhao, Y. Li, W. Li, Y. Q. Wu and L. X. Wu, *Langmuir*, 2010, **26**, 18430–18436.

49 Z. L. Zhang, L. Zhou, Y. Q. Zhou, J. Y. Liu, X. Y. Xing, J. Zhong, G. L. Xu, Z. H. Kang and J. Liu, *Biomaterials*, 2015, **65**, 56–65.

50 K. N. Raymond and V. C. Pierre, *Bioconjugate Chem.*, 2005, **16**, 3–8.

51 Y. L. Wang, S. Y. Zhou, D. L. Kong, H. S. Yang, W. Q. Chai, U. Kortz and L. X. Wu, *Dalton Trans.*, 2012, **41**, 10052–10059.

52 S. M. Zhang, Y. M. Zheng, D. Y. Fu, W. Li, Y. Q. Wu, B. Li and L. X. Wu, *J. Mater. Chem. B*, 2017, **5**, 4035–4043.

53 J. H. Feng, X. J. Li, F. K. Pei, G. Y. Sun, X. Zhang and M. L. Liu, *Magn. Reson. Imaging*, 2002, **20**, 407–412.

54 D. L. Kong, B. Wei, S. Y. Zhou, H. S. Yang and Y. Jiang, *Chem. Res. Chin. Univ.*, 2013, **29**, 1055–1058.

55 J. H. Feng, G. Y. Sun, F. K. Pei and M. L. Liu, *J. Inorg. Biochem.*, 2002, **92**, 193–199.

56 W. Q. Chai, S. Wang, H. Zhao, G. F. Liu, K. Fischer, H. L. Li, L. X. Wu and M. Schmidt, *Chem. – Eur. J.*, 2013, **19**, 13317–13321.

57 J. Ly, Y. H. Li, M. N. Vu, B. A. Moffat, K. S. Jack, J. F. Quinn, M. R. Whittaker and T. P. Davis, *Nanoscale*, 2018, **10**, 7270–7280.

58 R. B. Lauffer, *Chem. Rev.*, 1987, **87**, 901–927.

59 Y.-W. Jun, J.-H. Lee and J. Cheon, *Angew. Chem., Int. Ed.*, 2008, **47**, 5122–5135.

60 J.-s. Choi, J.-H. Lee, T.-H. Shin, H.-T. Song, E. Y. Kim and J. Cheon, *J. Am. Chem. Soc.*, 2010, **132**, 11015–11017.

61 Y. L. Wang, W. Li, S. Y. Zhou, D. L. Kong, H. S. Yang and L. X. Wu, *Chem. Commun.*, 2011, **47**, 3541–3543.

62 K. De Clercq, E. Persoons, T. Napso, C. Luyten, T. N. Parac-Vogt, A. N. Sferruzzi-Perri, G. Kerckhofs and J. Vriens, *Proc. Natl. Acad. Sci. U. S. A.*, 2019, **116**, 13927–13936.

63 G. Kerckhofs, S. Stegen, N. van Gastel, A. Sap, G. Falgayrac, G. Penel, M. Durand, F. P. Luyten, L. Geris, K. Vandamme, T. Parac-Vogt and G. Carmeliet, *Biomaterials*, 2018, **159**, 1–12.

64 L. Y. Zong, H. X. Wu, H. Lin and Y. Chen, *Nano Res.*, 2018, **11**, 4149–4168.

65 S. M. Zhang, Y. M. Zheng, S. Y. Yin, J. Z. Sun, B. Li and L. X. Wu, *Chem. – Eur. J.*, 2017, **23**, 2802–2810.

66 S. Link and M. A. El-Sayed, *Int. Rev. Phys. Chem.*, 2000, **19**, 409–453.

67 J. R. Lepock, *Int. J. Hyperthermia*, 2003, **19**, 252–266.

68 J. R. Melamed, R. S. Edelstein and E. S. Day, *ACS Nano*, 2015, **9**, 6–11.

69 J. G. Short and P. F. Turner, *Proc. IEEE*, 1980, **68**, 133–142.

8204 | *J. Mater. Chem. B*, 2020, **8**, 8189–8206

This journal is © The Royal Society of Chemistry 2020

70 J. A. Dickson and S. K. Calderwood, *Ann. N. Y. Acad. Sci.*, 1980, **335**, 180–205.

71 D. K. Roper, W. Ahn and M. Hoepfner, *J. Phys. Chem. C*, 2007, **111**, 3636–3641.

72 W. Ahn and D. K. Roper, *J. Phys. Chem. C*, 2008, **112**, 12214–12218.

73 Q. W. Tian, F. R. Jiang, R. J. Zou, Q. Liu, Z. G. Chen, M. F. Zhu, S. P. Yang, J. L. Wang, J. H. Wang and J. Q. Hu, *ACS Nano*, 2011, **5**, 9761–9771.

74 R. I. Buckley and R. J. H. Clark, *Coord. Chem. Rev.*, 1985, **65**, 167–218.

75 N. S. Hush, *Prog. Inorg. Chem.*, 1967, **8**, 391–444.

76 L. Y. Zhao, Y. M. Liu, R. Chang, R. R. Xing and X. H. Yan, *Adv. Funct. Mater.*, 2019, **29**, 1806877.

77 A. Müller and C. Serain, *Acc. Chem. Res.*, 2000, **33**, 2–10.

78 B.-L. Fei, N.-P. Deng, J.-H. Wang, Q.-B. Liu, J.-Y. Long, Y.-G. Li and X. Mei, *J. Hazard. Mater.*, 2017, **340**, 326–335.

79 A. Müller, M. T. Pope, A. M. Todea, H. Bögge, J. van Slageren, M. Dressel, P. Gouzerh, R. Thouvenot, B. Tsukerblat and A. Bell, *Angew. Chem., Int. Ed.*, 2007, **46**, 4477–4480.

80 A. Müller, M. Koop, H. Bögge, M. Schmidtmann and C. Beugholt, *Chem. Commun.*, 1998, 1501–1502.

81 A. Müller, B. Botar, H. Bögge, P. Kögerler and A. Berkle, *Chem. Commun.*, 2002, 2944–2945.

82 Y. C. Wang, F. Y. Li, N. Jiang, X. Z. Liu and L. Xu, *Dalton Trans.*, 2019, **48**, 14347–14353.

83 Y. Yong, L. J. Zhou, S. S. Zhang, L. Yan, Z. J. Gu, G. J. Zhang and Y. L. Zhao, *NPG Asia Mater.*, 2016, **8**, e273.

84 E. Haviv, L. J. W. Shimon and R. Neumann, *Chem. – Eur. J.*, 2017, **23**, 92–95.

85 A. Albanese, P. S. Tang and W. C. W. Chan, *Annu. Rev. Biomed. Eng.*, 2012, **14**, 1–16.

86 H. S. Choi, W. H. Liu, P. Misra, E. Tanaka, J. P. Zimmer, B. I. Ipe, M. G. Bawendi and J. V. Frangioni, *Nat. Biotechnol.*, 2007, **25**, 1165–1170.

87 R. K. Jain and T. Stylianopoulos, *Nat. Rev. Clin. Oncol.*, 2010, **7**, 653–664.

88 C. Zhang, W. B. Bu, D. L. Ni, C. J. Zuo, C. Cheng, Q. Li, L. L. Zhang, Z. Wang and J. L. Shi, *J. Am. Chem. Soc.*, 2016, **138**, 8156–8164.

89 A. L. Harris, *Nat. Rev. Cancer*, 2002, **2**, 38–47.

90 A. Verma, J. M. Simard, J. W. E. Worrall and V. M. Rotello, *J. Am. Chem. Soc.*, 2004, **126**, 13987–13991.

91 A. Solé-Daura, J. M. Poblet and J. J. Carbó, *Chem. – Eur. J.*, 2020, **26**, 5799–5809.

92 J. F. Li, Z. J. Chen, M. C. Zhou, J. B. Jing, W. Li, Y. Wang, L. X. Wu, L. Y. Wang, Y. Q. Wang and M. Lee, *Angew. Chem., Int. Ed.*, 2016, **55**, 2592–2595.

93 L. Vandebroek, E. De Zitter, H. G. T. Ly, D. Conić, T. Mihaylov, A. Sap, P. Proost, K. Pierloot, L. Van Meervelt and T. N. Parac-Vogt, *Chem. – Eur. J.*, 2018, **24**, 10099–10108.

94 F. Xue, Y. B. Zhang, F. W. Zhang, X. M. Ren and H. Q. Yang, *ACS Appl. Mater. Interfaces*, 2017, **9**, 8403–8412.

95 Y. Yang, B. Zhang, Y. Z. Wang, L. Yue, W. Li and L. X. Wu, *J. Am. Chem. Soc.*, 2013, **135**, 14500–14503.

96 S. C. Chai, X. Cao, F. R. Xu, L. Zhai, H. J. Qian, Q. Chen, L. X. Wu and H. L. Li, *ACS Nano*, 2019, **13**, 7135–7145.

97 S. M. Zhang, B. Peng, P. Y. Xue, X. P. Kong, Y. Tang, L. X. Wu and S. Y. Lin, *Soft Matter*, 2019, **15**, 5375–5379.

98 S. M. Zhang, H. B. Chen, G. H. Zhang, X. P. Kong, S. Y. Yin, B. Li and L. X. Wu, *J. Mater. Chem. B*, 2018, **6**, 241–248.

99 G. H. Zhang, B. Y. Li, Y. Zhou, X. F. Chen, B. Li, Z.-Y. Lu and L. X. Wu, *Nat. Commun.*, 2020, **11**, 425.

100 J. H. Zhou, W. C. Zhao, Z. H. Miao, J. G. Wang, Y. Ma, H. T. Wu, T. D. Sun, H. S. Qian and Z. B. Zha, *ACS Nano*, 2020, **14**, 2126–2136.

101 M. M. Ma, N. Gao, Y. H. Sun, X. B. Du, J. S. Ren and X. G. Qu, *Adv. Healthcare Mater.*, 2018, **7**, 1800320.

102 M.-F. Tsai, S.-H. G. Chang, F.-Y. Cheng, V. Shanmugam, Y.-S. Cheng, C.-H. Su and C.-S. Yeh, *ACS Nano*, 2013, **7**, 5330–5342.

103 X. G. Ding, C. H. Liow, M. X. Zhang, R. J. Huang, C. Y. Li, H. Shen, M. Y. Liu, Y. Zou, N. Gao, Z. J. Zhang, Y. G. Li, Q. B. Wang, S. Z. Li and J. Jiang, *J. Am. Chem. Soc.*, 2014, **136**, 15684–15693.

104 T. O. McBride, B. W. Pogue, S. Poplack, S. Soho, W. A. Wells, S. D. Jiang, U. L. Osterberg and K. D. Paulsen, *J. Biomed. Opt.*, 2002, **7**, 72–79.

105 Y. Cai, Z. Wei, C. H. Song, C. C. Tang, W. Han and X. C. Dong, *Chem. Soc. Rev.*, 2019, **48**, 22–37.

106 Y. Lyu, J. C. Li and K. Y. Pu, *Small Methods*, 2019, **3**, 1900553.

107 A. Müller, E. Krickemeyer, J. Meyer, H. Bögge, F. Peters, W. Plass, E. Diemann, S. Dillinger, F. Nonnenbruch, M. Randerath and C. Menke, *Angew. Chem., Int. Ed. Engl.*, 1995, **34**, 2122–2124.

108 G. Y. Liu, J. W. Zhu, H. Guo, A. H. Sun, P. Chen, L. Xi, W. Huang, X. J. Song and X. C. Dong, *Angew. Chem., Int. Ed.*, 2019, **58**, 18641–18646.

109 Y. H. Shi, J. J. Zhang, H. Huang, C. Y. Cao, J. J. Yin, W. J. Xu, W. J. Wang, X. J. Song, Y. W. Zhang and X. C. Dong, *Adv. Healthcare Mater.*, 2020, **9**, 2000005.

110 C. G. A. Hoelen and F. F. M. de Mul, *Appl. Opt.*, 2000, **39**, 5872–5883.

111 X. D. Wang, G. Ku, M. A. Wegiel, D. J. Bornhop, G. Stoica and L. V. Wang, *Opt. Lett.*, 2004, **29**, 730–732.

112 I. Steinberg, D. M. Huland, O. Vermesh, H. E. Frostig, W. S. Tummers and S. S. Gambhir, *Photoacoustics*, 2019, **14**, 77–98.

113 T. R. Zhao, A. E. Desjardins, S. Ourselin, T. Vercauteren and W. F. Xia, *Photoacoustics*, 2019, **16**, 100146.

114 L. G. Tang, F. Yu, B. W. Tang, Z. Yang, W. P. Fan, M. R. Zhang, Z. T. Wang, O. Jacobson, Z. J. Zhou, L. Li, Y. J. Liu, D. O. Kiesewetter, W. Tang, L. C. He, Y. Ma, G. Niu, X. Z. Zhang and X. Y. Chen, *ACS Appl. Mater. Interfaces*, 2019, **11**, 27558–27567.

115 Y.-F. Xiao, F.-F. An, J.-X. Chen, J. Yu, W.-W. Tao, Z. Q. Yu, R. Ting, C.-S. Lee and X.-H. Zhang, *Small*, 2019, **15**, 1903121.

116 D. L. Ni, D. W. Jiang, H. F. Valdovinos, E. B. Ehlerding, B. Yu, T. E. Barnhart, P. Huang and W. B. Cai, *Nano Lett.*, 2017, **17**, 3282–3289.

117 Z. Yang, W. P. Fan, W. Tang, Z. Y. Shen, Y. L. Dai, J. B. Song, Z. T. Wang, Y. Liu, L. S. Lin, L. L. Shan, Y. J. Liu,

This journal is © The Royal Society of Chemistry 2020

J. Mater. Chem. B, 2020, **8**, 8189–8206 | **8205**

O. Jacobson, P. F. Rong, W. Wang and X. Y. Chen, *Angew. Chem., Int. Ed.*, 2018, **57**, 14101–14105.

118 X. Zhang, Z. Q. Xi, J. O. Machuki, J. J. Luo, D. Z. Yang, J. J. Li, W. B. Cai, Y. Yang, L. J. Zhang, J. W. Tian, K. J. Guo, Y. Y. Yu and F. L. Gao, *ACS Nano*, 2019, **13**, 5306–5325.

119 R. D. Issels, *Eur. J. Cancer*, 2008, **44**, 2546–2554.

120 K. F. Chu and D. E. Dupuy, *Nat. Rev. Cancer*, 2014, **14**, 199–208.

121 Y. Lyu, D. Cui, H. Sun, Y. S. Miao, H. W. Duan and K. Y. Pu, *Angew. Chem., Int. Ed.*, 2017, **56**, 9155–9159.

122 A. Ito, M. Shinkai, H. Honda, K. Yoshikawa, S. Saga, T. Wakabayashi, J. Yoshida and T. Kobayashi, *Cancer Immunol. Immunother.*, 2003, **52**, 80–88.

123 H. Lin, S. S. Gao, C. Dai, Y. Chen and J. L. Shi, *J. Am. Chem. Soc.*, 2017, **139**, 16235–16247.

124 J. P. May and S.-D. Li, *Expert Opin. Drug Delivery*, 2013, **10**, 511–527.

125 J. T. Xu, W. Han, T. Jia, S. M. Dong, H. T. Bi, D. Yang, F. He, Y. L. Dai, S. L. Gai and P. P. Yang, *Chem. Eng. J.*, 2018, **342**, 446–457.

126 J. T. Xu, W. Han, Z. Y. Cheng, P. P. Yang, H. T. Bi, D. Yang, N. Niu, F. He, S. L. Gai and J. Lin, *Chem. Sci.*, 2018, **9**, 3233–3247.

127 S. K. Liu, W. T. Li, S. L. Gai, G. X. Yang, C. N. Zhong, Y. L. Dai, F. He, P. P. Yang and Y. D. Suh, *Biomater. Sci.*, 2019, **7**, 951–962.

128 Q. J. He, *Biomater. Sci.*, 2017, **5**, 2226–2230.

129 R. Motterlini and L. E. Otterbein, *Nat. Rev. Drug Discovery*, 2010, **9**, 728–743.

130 W. Tang, W. P. Fan, Z. T. Wang, W. Z. Zhang, S. Y. Zhou, Y. J. Liu, Z. Yang, E. Shao, G. F. Zhang, O. Jacobson, L. L. Shan, R. Tian, S. Y. Cheng, L. S. Lin, Y. L. Dai, Z. Y. Shen, G. Niu, J. Xie and X. Y. Chen, *ACS Nano*, 2018, **12**, 12269–12283.